In situ characterization of laser-generated melt pools using synchronized ultrasound and high-speed X-ray imaging[a) FREE]

Jared Gillespie; Wei Yi Yeoh; Cang Zhao; Niranjan D. Parab; Tao Sun; Anthony D. Rollett; Bo Lan; Christopher M. Kube

Check for updates

View Online   Export Citation   CrossMark
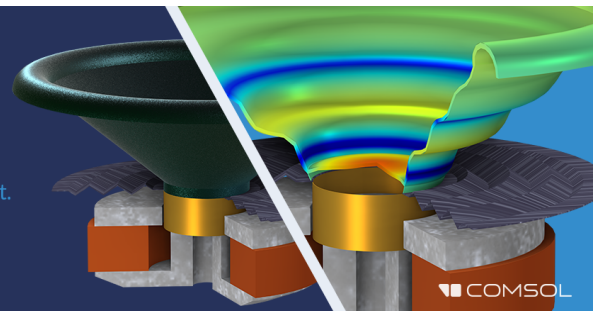
In situ characterization of laser-generated melt pools using synchronized ultrasound and high-speed X-ray imaging[a)]

Jared Gillespie,[1] Wei Yi Yeoh,[2] Cang Zhao,[3,b)] Niranjan D. Parab,[3,c)] Tao Sun,[3,d)] Anthony D. Rollett,[4,e)] Bo Lan,[2] and Christopher M. Kube[1,f)]

[1]*Department of Engineering Science and Mechanics, The Pennsylvania State University, University Park, Pennsylvania 16802, USA*

[2]*Department of Mechanical Engineering, Imperial College London, Exhibition Road, London SW7 2AZ, United Kingdom*

[3]*X-ray Science Division, Argonne National Laboratory, Lemont, Illinois 60439, USA*

[4]*Department of Materials Science and Engineering, Carnegie Mellon University, Pittsburgh, Pennsylvania 15213, USA*

ABSTRACT:

Metal additive manufacturing is a fabrication method that forms a part by fusing layers of powder to one another. An energy source, such as a laser, is commonly used to heat the metal powder sufficiently to cause a molten pool to form, which is known as the melt pool. The melt pool can exist in the conduction or the keyhole mode where the material begins to rapidly evaporate. The interaction between the laser and the material is physically complex and difficult to predict or measure. In this article, high-speed X-ray imaging was combined with immersion ultrasound to obtain synchronized measurements of stationary laser-generated melt pools. Furthermore, two-dimensional and three-dimensional finite-element simulations were conducted to help explain the ultrasonic response in the experiments. In particular, the time-of-flight and amplitude in pulse-echo configuration were observed to have a linear relationship to the depth of the melt pool. These results are promising for the use of ultrasound to characterize the melt pool behavior and for finite-element simulations to aid in interpretation. © *2021 Acoustical Society of America.*
https://doi.org/10.1121/10.0006386

I. INTRODUCTION

Metal additive manufacturing (AM) is generally described as a layer-by-layer manufacturing process in which an energy source, such as a laser or electron beam, is used to fuse a feedstock material, such as powder or wire, to a previous layer or substrate. Laser powder bed fusion (L-PBF) and directed energy deposition (DED) are common AM techniques that typically rely on a laser energy source to melt a localized region during the joining process. The resulting liquefied region is referred to as a melt pool. The formation, behavior, and solidification of the melt pool dictate the material microstructure and, thus, greatly influence the resultant properties and performances of the AM parts.[1,2] For example, influencing the melt pool through the optimization of process parameters, such as laser speed and power, has led to parts with better tensile strength over the wrought equivalents.[3]

Melt pools generated during the AM process exist in either the conduction or the keyhole mode. The former exists when the material is heated to a liquid phase via conduction of the laser or electron beam heat flux on the surface. The latter exists when the energy density of the laser is sufficient to cause evaporation from the melt pool. The evaporation causes a vapor depression, or keyhole, to form. The keyhole effectively enhances the laser absorption and can lead to instability and collapse of the keyhole, trapping gas within the material and resulting in porosity.[4,5] Furthermore, keyholing has been correlated with producing other undesirable defects in AM parts such as surface roughness[1] and hot tearing or hot cracking, resulting from high temperature gradients of the keyhole.[6,7] It is noted that keyholing is common in laser welding applications as well. However, the extremely high cooling rates, laser speeds, and differences in the thermal properties of the surrounding host material result in melt pools with sizes, dynamic behavior, solidification, and microstructures that are different from those found in laser welding. In order to allow AM to be adopted for structural applications, such as the aerospace industry, these defects must be eliminated.[8]

To this end, optimal AM process parameters are usually sought to eliminate defects such as porosity, which can stem from the dynamics of an unstable keyhole. Often, some combination of the laser power and scan speed are employed to maintain the power density beneath the threshold that

---

keyholing will occur.[9] However, reducing the power density has its own complications as the lack of fusion defects and balling can occur. Thus, the combinations of optimal process parameters to avoid all such defects can span a small range of process variables known as the *process window*.[10] In principle, absolute determination of the process window would remove the probability of defect formation in AM parts. However, the process window is greatly influenced by several confounding variables, such as feedstock properties, material selection, and machine variability, during the build. In some instances, the process window can be extremely small such that keyhole formation is inevitable.[9]

The determination of the process window is extremely challenging when printing with new or difficult-to-print materials. Multi-scale models have been developed in the attempt to aid this process by predicting the subsurface melt pool behavior in AM parts. However, the interactions involved in the complex physical phenomena present make it incredibly challenging to computationally capture the exact melt pool behavior. Therefore, models generally rely on limiting assumptions, which limits their application. Furthermore, for many of these models, inputs from experimental measurements of the melt pool behavior are currently needed for training and validation.[11] Therefore, being able to monitor melt pool behavior, including formation and solidification, is a potentially invaluable tool for advancing AM. Many methods, such as high-speed optical imaging or infrared imaging, are able to characterize the cross section of the melt pools present at the top-most layer of a print. However, these methods have limited sensitivity to dynamics occurring beneath the surface.[12] Han *et al.* did demonstrate the feasibility of acoustic resonance methods for determining the melt pool depth and size using a low melting point (70 °C) metal placed into drilled flat bottom holes.[13]

Recently, high-speed X-ray imaging has been used to closely study the subsurface melt pool and keyholing phenomena in real time.[5] Full-field propagation-based X-ray imaging is sensitive to the inhomogeneities caused by variations in the absorption of the material. Consequently, the melt pools can be imaged as the absorption from the liquid and gaseous phases are distinct from the solid phase. Thus, the phase boundaries are discernible, allowing high-speed X-ray imaging to capture the highly dynamic melt pool behavior.[5,9,14–18] Besides melt pool geometry, features such as spatter motion,[5,18] solidification rate,[5] phase-transformation,[5] vapor depression,[14] pore formation,[17,19] and hot cracking[7,9] have been observed. Whereas high-power X-ray imaging is effective in studying laser-generated melt pools, the limited availability and lack of portability inhibits the ability to monitor melt pools beyond the laboratory settings.[20] Ultrasound represents an alternate technique to sense melt pool dynamics and associated features on solidification.[21]

Ultrasound is known to scatter from inhomogeneities characterized by local variations in the density and/or elastic stiffness.[22] In the case of the melt pool, as the material transitions to a liquid phase, the shear modulus is asymptotically reduced to zero. Such an impedance mismatch indicates that shear waves will not propagate into the melt pool between the solid-phase base metal and the liquid-phase melt pool. Furthermore, it is expected that shear waves will have a high scattering amplitude near the solid-liquid transition region, enhancing the sensitivity. Such a transition region exists for both conduction and keyhole mode melt pools and, as a result, scattering from the melt pool is expected to be sensitive to either mode. In addition to the material properties, ultrasonic scattering also depends on the geometry and size of the inhomogeneity.[22] Therefore, the size and shape of the melt pool are expected to influence the ultrasonic scattering. Furthermore, previous research was able to observe a correlation between the ultrasonic scattering amplitudes and the depth and width of the melt pool.[21] Hence, ultrasound will likely be sensitive to the geometry of the melt pool and even the mode of the melt pool.

In the current work, results from the synchronized high-speed X-ray imaging, immersion ultrasonic scattering from the melt pool, and finite-element modeling results are reported. Unlike the previous measurements using acoustic resonance methods,[13] the experiments are conducted on realistic laser-generated melt pools on the surface of an Al6061 substrate, which exhibit melt pool dynamics found in actual AM processes. The overall goal is to integrate these tools to provide answers to open questions involving melt pools in relation to AM process windows. Eventually, the described ultrasonic method is to be transitioned into individual printers to help establish process windows at a local level. In such cases, the method will be most applicable to observing and studying the melt pool phenomena occurring in simple passes over the build substrate or initial stages of a part build. While of interest, a different ultrasound configuration would need to be explored to extend the method toward monitoring the melt pools throughout an entire build. The present results represent the first synchronized acquisition of ultrasound and high-speed X-ray imaging, which is the first step toward the overall goal. Both X-ray imaging and finite-element modeling were used to validate and confirm the sensitivity between ultrasonic scattering and melt pool behavior.

II. SYNCHRONIZED ULTRASOUND AND HIGH-SPEED X-RAY IMAGING

In previous work,[21] ultrasonic scattering measurements were conducted on melt pools generated on the surface of a stainless steel (SS430) plate using a laser welder. Correlations were established between the scattering amplitude and melt pool width and depth based on destructive sectioning and optical microscopy. However, questions remained regarding the sensitivity of ultrasound to melt pool features that are unique to traditional metal AM processes as opposed to melt pools generated with the higher laser power used in laser welding. Furthermore, the exact behavior of the melt pool dynamics was unknown and had to be inferred afterward from optical microscopy. As a result, the dynamic

ultrasonic behavior was unable to be directly attributed to the rapid changes in the melt pool dimensions. To answer these open questions, experiments at the Advanced Photon Source at Argonne National Laboratory were conducted to provide synchronized ultrasonic scattering and high-speed X-ray imaging measurements. The synchronized measurements, in addition to the finite-element simulations described in Sec. III, provide the needed ground truth to understand how the melt pool dynamics influence the ultrasonic response.

A. Experimental configuration

A number of special considerations were made in the experimental configuration to enhance the interaction of the ultrasonic field with the melt pool. First, bulk shear waves were chosen as the incident wave field because of their greater propensity to scattering from the solid-liquid boundary of the melt pool. Focused ultrasonic immersion-style transducers were used to generate longitudinal bulk waves into a water medium as seen in Figs. 1(a) and 1(b). Second, an incident angle of $\theta_i = 21.12°$ with respect to the sample normal was used. This angle is beyond the first critical angle for the water and material (Al6061) interface and, thus, generates a strong mode-converted shear wave into the sample. Using Snell's law, the given incident angle will produce a refracted shear wave propagating at an angle of $\theta_r = 45°$ within the sample, which is along the radial dimension for an approximately hemispherical melt pool. Additionally, a second transducer with identical parameters was placed on the opposite side of the sample with the midsection of the sample serving as a mirror plane. Having a pair of transducers allows for either pulse-echo (PE) measurements, in which a single transducer acts as a transmitter and receiver, or pitch-catch (PC) measurements, in which the transducer transmits while the other receives. Both transducers had a center frequency of 25 MHz, nominal diameter of 6.35 mm, geometric focal length of 25.4 mm, and measured focal lengths of 26.1 mm and 26.2 mm, respectively, using a hydrophone in water. Based on the measured focal length, the geometric ray theory[22] was used to select a water path

d_w of 19.49 mm to achieve a desired material path d_m of 3.37 mm to a radial distance d from the laser source as shown in Fig. 1(b). Based on these considerations, the focal point in the material was calculated to be a radial distance $d = 168\ \mu m$ from the laser source. Therefore, a melt pool extending between 100 and 200 μm in depth will –cross into the focal zone of the transducer. Furthermore, the 25 MHz center frequency gives a shear wavelength of 116.6 μm in the Al6061 sample, which is on the order of the characteristic dimensions of the melt pools observed. It is noted that the water level is kept approximately 0.5 mm beneath the top surface of the sample. Hence, while the ultrasonic transducers are completely immersed, the ultrasonic field within the sample reaches above the maximum water level, scatters from the melt pool, and propagates to the transducers.

The excitation and reception of the ultrasonic transducers were controlled using a dual channel ultrasonic pulser-receiver *JSR DPR-500* (Pittsford, NY). The piezoelectric element within the transducer was excited by a 300 V negative spike with a duration of 10 ns. The excitation causes the element to ring at its center frequency. Immediately after excitation, the pulser-receiver switches into reception mode. The rate of excitation is controlled via a user interface by setting the pulse-rate-frequency (PRF) parameter, which controls the frequency of the internal oscillator within the pulse-receiver. The PRF is limited by the time-of-flight (TOF) of the ultrasound to scatter from the melt pool and be received by the transducer. For example, an individual ultrasound pulse requires approximately 28 μs to propagate from the transducer to the melt pool and back from the melt pool to the transducer. Thus, a PRF of 28.5 kHz was selected, which causes the pulser-receiver to be in reception mode for 35.1 μs (the inverse of the PRF). Increasing the PRF further would cause previous pulses to interfere with the acquisition. In other words, the current configuration allowed for 28.5 waveforms to be acquired every 1 ms. Therefore, hundreds of ultrasound waveforms can be collected when a melt pool exists for only a few milliseconds.

The received ultrasonic response passes through the pulser-receiver and is filtered and output to the digitizer card
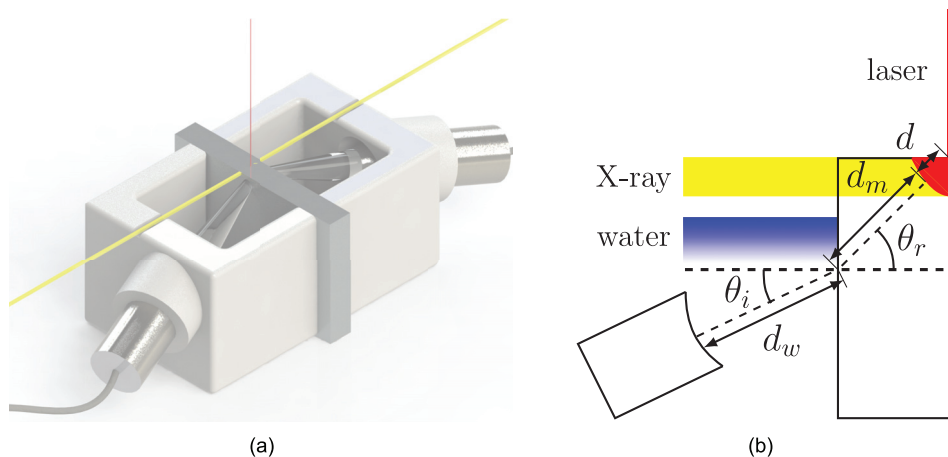
(a)

(b)

FIG. 1. (Color online) The (a) rendering of the 3D printed fixture to hold the ultrasound transducers and sample and (b) schematic of the incident and refracted ray paths.

J. Acoust. Soc. Am. **150** (4), October 2021

Gillespie *et al.*   2411

NI PXIe-5162 within a National Instruments chassis *NI PXIe-1071* and controller *NI PXIe-8880* (Austin, TX). Acquisition is initiated by the digitizer through a 3 V trigger pulse output by the pulser-receiver and synchronized according to the PRF. Thus, the digitizer is armed at precisely the instant when the transducer generates a pulse. A delay of $25\,\mu s$ was set to capture only the portion of the ultrasonic waveform containing the scattering from the melt pool. This portion of the signal was captured by acquiring 5000 time-amplitude data points at a sampling rate of 500 MHz and stored into the on-board memory. The digitizer was limited to a voltage of ± 1.2 V to increase the vertical resolution. Hence, the time-windowed region containing the useful ultrasonic response was between 25 and $35\,\mu s$. The digitizer was disarmed after acquiring the 5000 data points until it received subsequent trigger pulses.

The X-ray images were captured using a high-speed camera *Photron FastCam SA-Z* (Tokyo). The imaging frame rate was set to 28.503 kHz and synchronized with the ultrasonic PRF. The camera recorded 896×776 pixel images with a spatial resolution of $1.923\,\mu m$/pixel. The synchronization of the high-speed camera to the ultrasonic provided an image to be captured at a precise time interval when the ultrasound scatters from the melt pool. The melt pools were generated using a stationary 1070 nm fiber laser producing a $120\,\mu m$ diameter Gaussian beam. The melt pools were generated by activating the laser for a duration of 5 ms with a laser power of 477 W. The sample was adjusted after each melt pool was generated such that the heat-affected regions from the previous experiments did not impact subsequent experiments.

B. Materials

Samples of the aluminum alloy (Al6061-T651) were selected for the measurements. Such alloys are highly desirable as structural parts in various applications as they often provide a suitable balance between the weight and mechanical properties. Common aluminum alloys, such as Al6061 and AlSi10Mg, present several challenges in AM. The initial laser absorptivity is generally low and in the range 0.1–0.2, but is strongly dependent on the laser power and material behavior during heating due to the phase dependency and interaction with oxides.[23] During initial surface melting, material evaporation can cause keyhole formation which improves the laser absorptivity, resulting in an increase in the melt pool depth. Furthermore, during solidification of the melt pool, extremely high cooling rates exist on the order of $10^6\,K/s$.[24] These cooling rates can cause significant thermal stresses and subsequent crack formation (hot cracking) in some aluminum alloys.[7,25] Thus, the choice of Al6061 samples affords the possibility of sensing several interesting structural dynamics including keyhole initiation and fluctuation, pore formation, solidification, and hot cracking.

A total of six samples having dimensions of $101.6 \times 25.4 \times 4.762$ mm were sectioned from two 304.8×25.4 $\times 4.762$ mm precision ground bars. Prior to the precision grinding by the supplier, the Al6061 alloy was cold rolled from a cast ingot and heat treated to a T651 temper. The alloy composition met ASTM standard E1251. The sectioned sample faces were polished to a mirror finish using sandpaper and completed with a $0.1\,\mu m$ diamond slurry. The standard ultrasonic wave velocity measurements were performed to obtain the longitudinal and shear wave velocities of $v_L = 6207$ m/s and $v_T = 2916$ m/s, respectively. These wave velocities were used to aid the design of the experimental ultrasound configuration and optimize sensitivity to the melt pools formed near the top surface of the sample and within the sample's midplane as seen in Figs. 1(a) and 1(b).

C. Experimental results

The recorded X-ray images were post-processed using the open-source software, *ImageJ*.[26] Each frame was elementally divided by the pixel-intensities of a static X-ray frame captured prior to the laser being activated. By performing this division, the X-ray images are effectively normalized as the undesired image artifacts areremoved and the contrast of the dynamic structures is improved.

Each of the ultrasound time-amplitude waveforms were arranged sequentially, resulting in an ultrasound time history from before, during, and after the laser was activated. The results from two subsequent measurements are shown in Figs. 2(a) and 2(b). The first measurement as seen in Fig. 2(a) corresponds to a PC configuration, whereas Fig. 2(b) corresponds to a PE configuration. The two measurements were not made simultaneously; rather, the sample was slightly translated between the measurements such that the following measurement produced a melt pool in a new location. The laser power and duration were the same in both measurements. Figures 2(a) and 2(b) show the rectified ultrasound time history along with selected frames from the X-ray video. The full video results can be viewed in the supplementary files.[27]

Several observations can be made. Whereas the identical laser parameters were used, the melt pool behavior seen in the X-ray images in Figs. 2(a) and 2(b) varies significantly between the two experiments. The difference is thought to be caused by slightly different surface conditions, which influenced the laser absorption. Furthermore, the variability indicates the general unstable character of the keyhole melt pools in this material and supports the need for *in situ* monitoring. Even with the different melt pool behavior, both melt pools reach a similar depth of approximately $400\,\mu m$ in both experiments. As the melt pool increases in depth, the TOF of the ultrasound decreases. From a geometric standpoint, the shift in the TOF is expected as an increase in the melt pool results in a shortening of the travel path of the ultrasonic wave.

The melt pool and keyhole depth were then extracted from the high-speed X-ray images manually using *ImageJ*. Although other research has been able to use automatic geometry extraction,[5] the material and sample thickness
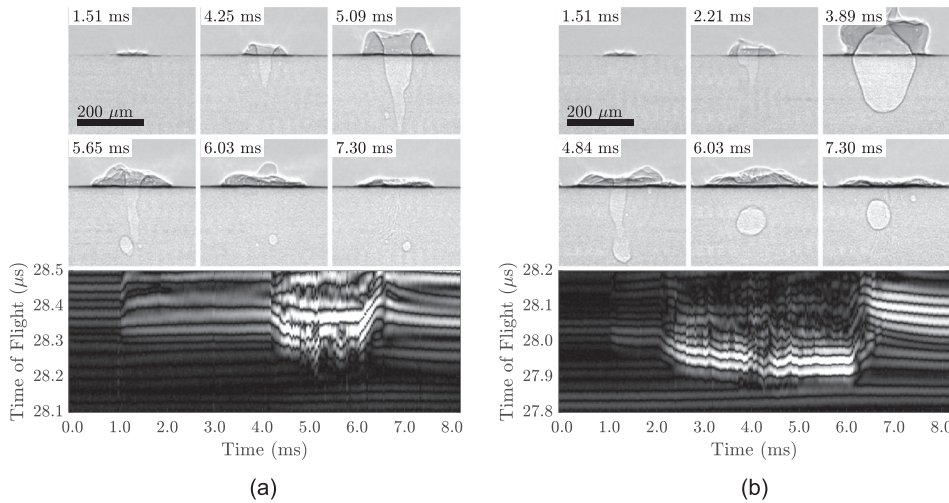
FIG. 2. The selected X-ray frames and ultrasound time history from the (a) PC and (b) PE configurations. For the ultrasound response, the amplitudes scale from low (red) to high (white). The laser was on during the time period from 1 to 6 ms. The full video results can be found in the supplementary files (Ref. 27).

rendered these methods impractical for the current results. The melt pool and keyhole depths were measured four separate times using the PC results. The standard deviation of these measurements, shown as the shaded region in Fig. 3(a), was then used to gauge the precision or repeatability of the manual method. The measurement error was seen to be greater at the instances of melt pool and keyhole initiation. However, during keyholing, there was a smaller deviation for both the melt pool and keyhole depths. Specifically, there is an average standard deviation of ± 8.21 and $\pm 1.14\,\mu m$ for the melt pool and keyhole measurements, respectively.

After validating the depth procedure, a single measurement was taken of the X-ray images for the PE results, which are shown in Fig. 3(b). It was expected that the first or earliest high amplitude signal observed in the ultrasound time history corresponds to the scattering from the boundary of the melt pool. Therefore, a *MATLAB* script was written to compare the amplitude of the ultrasound response between waveforms and effectively trace the high amplitude scattering through the duration of the ultrasound time history. The results are shown in Figs. 4(a) and 4(b) for PC and PE, respectively.

Several observations can be made when comparing the melt pool depth measured from the X-ray images and the earliest high amplitude ultrasonic scattering [compare Figs. 4(a) and 4(c) with Figs. 4(b) and 4(d), respectively]. First, when the laser is activated at $t = 1\,\mu s$, there is a noticeable shift in the TOF for both configurations, which corresponds to the emergence of a melt pool of approximately $50–75\,\mu m$ in depth. However, whereas the PE configuration exhibits a decrease in the TOF initially, the PC configuration exhibits a slight increase in the TOF initially. The behavior for the PC case could be caused by the increase in temperature, which would decrease the ultrasound wave velocity. However, the temperature effects would have a similar influence for both PC and PE. It is possible that a slight asymmetry was present, caused by a slight misalignment of the transducers in the PC case. Second, both PC and PE measurements experience a decrease in the TOF of approximately 90 ns between the laser activating and the maximum melt pool depth being reached. This behavior corroborates well with the measured depth of the melt pool, which reached a similar depth of approximately $400\,\mu m$ for both experiments. Such a change results in an average decrease in the TOF of $4.44\,\mu m/ns$ for melt pool depths greater than $100\,\mu m$ for either configuration.

It is important to note that the experiments involve several interesting and complicated phenomena. First, the rapidly changing keyhole dimensions lead to ultrasonic signals
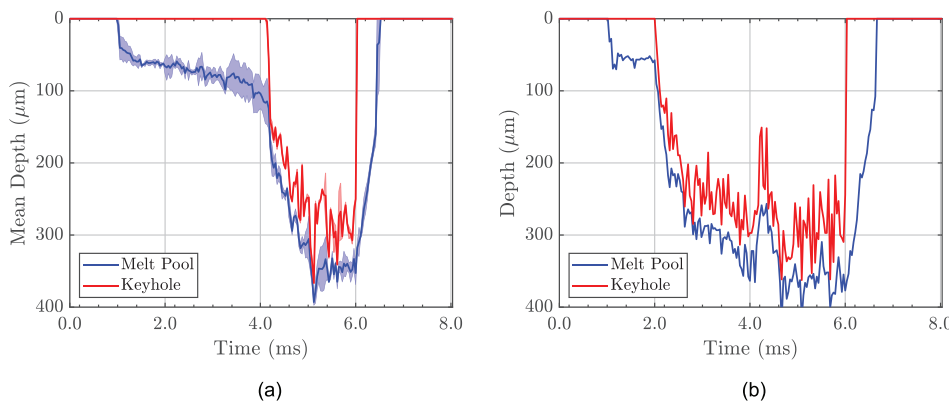

FIG. 3. (Color online) The melt pool and keyhole depths measured from the X-ray images for the (a) PC and (b) PE setups. The shaded regions surrounding the measurements in (a) represent the mean deviation taken from four separate measurements.

J. Acoust. Soc. Am. **150** (4), October 2021
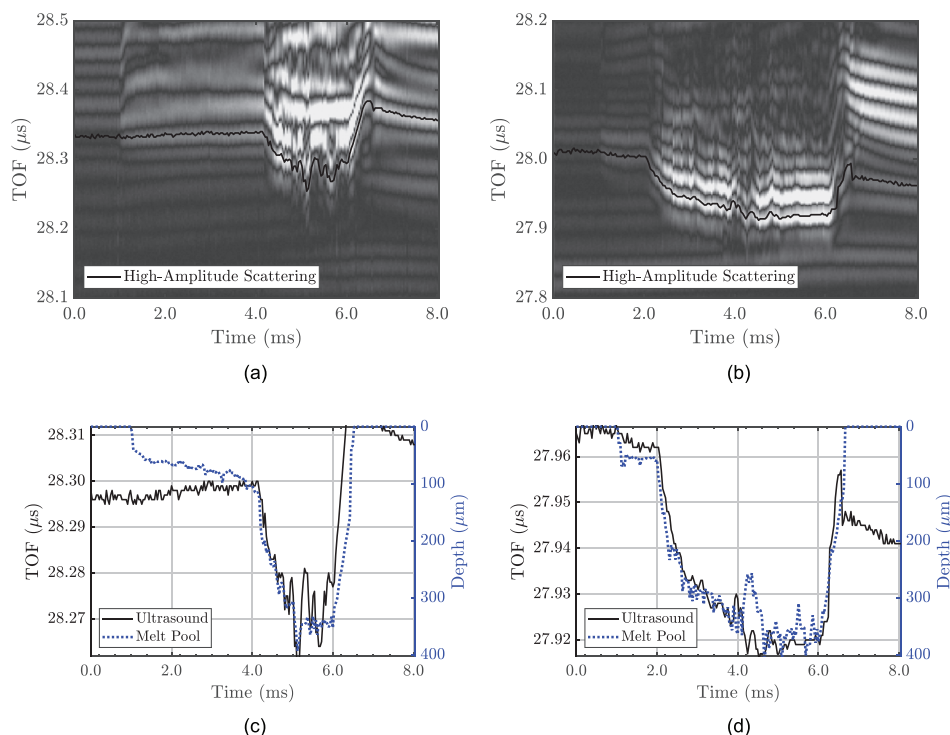
Gillespie *et al.* 2413

FIG. 4. (Color online) The ultrasound time history with the earliest high amplitude scattered signal for the (a) PC and (b) PE configurations compared with the melt pool depths in (c) and (d), respectively.

that, in turn, fluctuate rapidly in both configurations. A deterministic correlation between the keyhole and signals is required for the dynamic monitoring of the former. Second, the temperature gradient produced by the laser in the neighboring regions of the melt pool will affect the elastic properties of the sample, which, in turn, affect the propagation of the scattered wave. Furthermore, how the melt pool and keyhole physically interact and scatter ultrasound in both of the PC and PE configurations is not immediately obvious. These complexities are difficult to detect experimentally. Therefore, finite-element analysis (FEA) was used to create several models to help understand the interaction of the ultrasound with the melt pool and keyhole.

III. FEA

The FEA models were configured to resemble the experimental setup. However, three-dimensional (3D) models are computationally expensive due to the fine length scales of the features. Therefore, a simpler two-dimensional (2D) model was first used to investigate the potential effects of a liquid layer of the melt pool and heat-affected region before moving on to more complex 3D simulations. Two 25 MHz finite transducers are simulated to generate planar (2D) and focused (3D) shear waves at the incident angle of 45° to capture both of the PC and PE configurations for ultrasonic scattering from the melt pool.

A. 2D model

2D FEA models were generated using the commercial software package *Abaqus*.[28] These models were used to help understand open questions from the experiments, such as how temperature and the PC and PE configurations will affect the ultrasonic response. Liquid components and temperature gradients are computationally expensive to include in a 3D model, so they were first included in the 2D models to investigate their effect on the overall wave propagation. These findings were used to decide whether liquid and temperature could be omitted in the 3D simulations with a minimal reduction in accuracy.

The model setup is shown in Fig. 5, where the excitation and receiving surfaces are inclined at a 45° angle to generate 45° planar shear waves. A 4×8 mm model was used with a $40 \times 180 \mu$m cavity representing the keyhole. A liquid layer of 20μm was defined around the keyhole and is similar to what was observed in the experimental results. The propagation of the incident planar shear wave along with the scattered shear and mode-converted longitudinal waves are shown in Fig. 5. The scattered wave modes are observed to be separated in the time-domain and contain asymmetrical angular scattering amplitudes. These scattered signals are analogous to the time-of-flight diffraction (TOFD) method used for crack sizing, whereby the signals of interest originate from the diffraction by the tip of a crack and, in this case, can be used to estimate the keyhole depth.[29]

From this setup, the scattering from the melt pool and keyhole can be evaluated for both of the PC and PE configurations. To do so, three models are used with a liquid melt pool, a keyhole with a surrounding liquid layer, and a keyhole without a liquid layer. For each of these models, a constant temperature was assumed.

The PC and PE shear signals for all three models are shown in Fig. 6. For the PC configuration, all three models
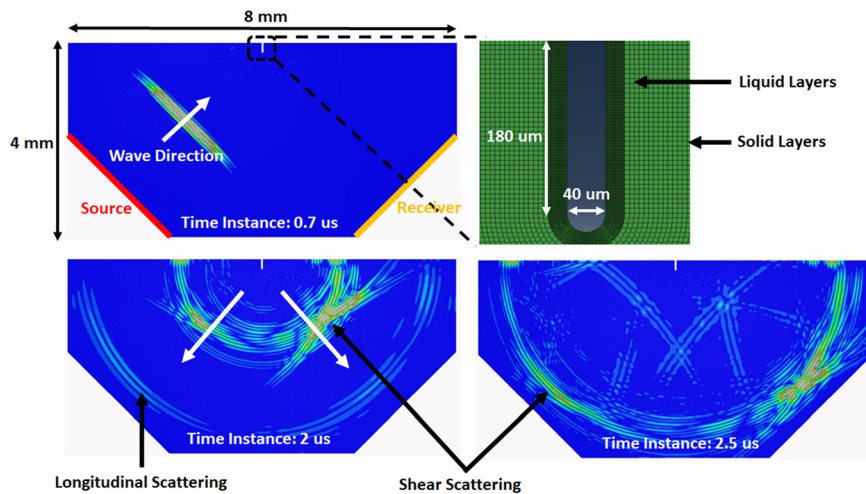
FIG. 5. (Color online) The 2D model schematic indicating the location of the source, receiver, and melt pool. The pool has a keyhole in the center and also contains both the solid and liquid layers and a varying temperature gradient to closely represent the experimental conditions.

result in comparable amplitudes and phase. For the PE configuration, the keyhole without a liquid layer generates the highest amplitude scattering. Additionally, unlike the PC configuration, there appears to be a phase shift between the models. A potential explanation for this difference is that the PE response includes not only the scattered signal but also the corner-reflected signals. Additionally, the increased impedance mismatch in the solid–cavity interface in the keyhole case causes a higher scattering amplitude. In the melt pool and liquid layer models, the liquid can cause additional mode-conversion at the solid-liquid boundary, which reduces the amplitude of the shear scattered signals. However, for the PC configuration, the scatterings have comparable contributions from the scattering, and the amplitude and phase variation is less significant between the models. It should be noted that because the models are in two dimensions, the transmitter and receiver are located in same plane, whereas in the experimental setup, the two transducers were not on the same plane. As a result, the received wave packets will contain reflections from the sample surface. Nonetheless, if the TOF is considered, small amplitude signals in the scattered response arrive at approximately the same time across the models at 2.70 and 2.72 μs for the PC and PE configurations, respectively. These results indicate that a transition between the melt pool and keyhole mode should have limited effects on the TOF of the early arrival

TOF, and the latter may be used for keyhole depth estimation.

Next, a varying temperature gradient surrounding the melt pool was considered. Two models with the same geometry as in Fig. 5 are compared: one with the temperature gradient in the solid layers and the other with the temperature being constant. The temperature gradient is indirectly implemented by sectioning the model into 5 μm layers, surrounding the melt pool with varying elastic properties and densities corresponding to the desired temperature of the region. These properties are obtained from the software *JMatPro*[30] by extrapolating the temperature-dependent density and elastic properties. Al6061 was not available in JmatPro, therefore, AL7075, a comparable alloy, was selected instead. These properties were assigned to a total of 200 layers to create a linearly decreasing temperature profile from 700 to 25 °C across the a 1 mm region surrounding the keyhole. The exact temperature profile in the experimental setup was not known and as a result, a linear distribution is assumed. Such a gradient is computationally expensive and unrealisic to be incorporated into 3D models. The temperature gradient corresponds to the shear velocity ranging from 2537 to 3087 m/s from the melting point ($T = 525$ °C) to room temperature and a longitudinal wave velocity varying from 4568 m/s at the melting point to 4468 m/s at 700 °C.
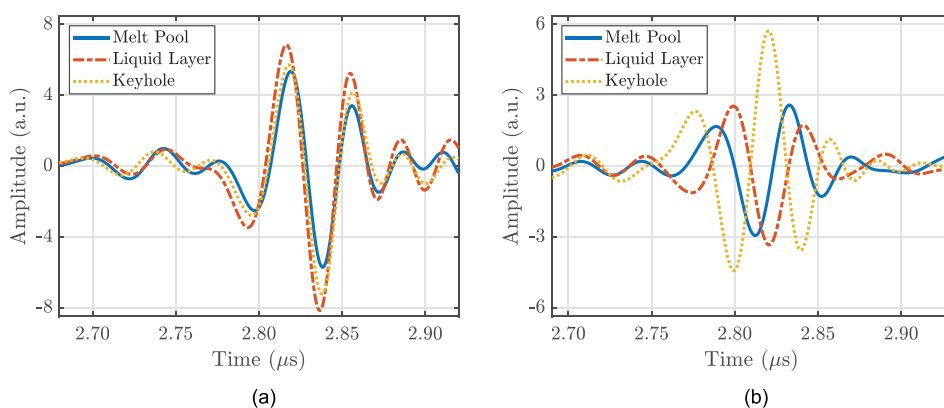

FIG. 6. (Color online) The (a) PC and (b) PE shear scattered signals for three models.

J. Acoust. Soc. Am. **150** (4), October 2021
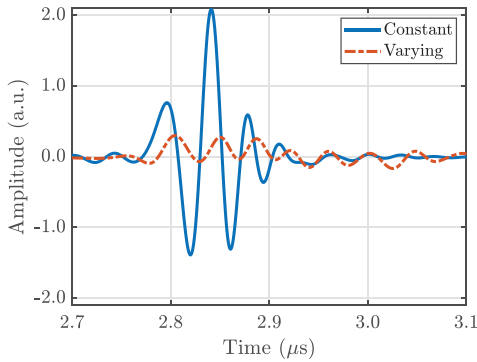
Gillespie *et al.*   2415

FIG. 7. (Color online) The time-domain signals of the shear scattered signals obtained from the 2D models with constant and varying temperature distributions.
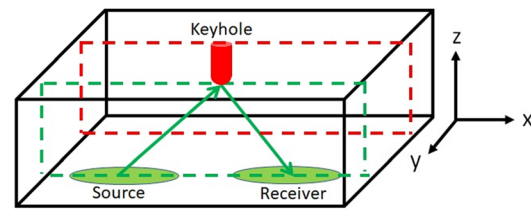

FIG. 8. (Color online) The finite element model configuration with the locations of the source, receiver and keyhole identified (image not to scale).

The resultant time-domain signals for both of the models are shown in Fig. 7. The scattered shear signal arrives earlier for the constant-temperature model because of the higher shear wave velocity at room temperature. The signal amplitude is also greater as a result of the larger impedance mismatch at the solid–liquid interface compared to the gradual change in the material properties because of the temperature gradient. Such a gradient not only affects the wave velocity, but also likely causes beam distortion because the temperature varies along and across the wavefront. Nevertheless, it is expected that a temperature gradient in the solid regions would be considerably more stable than the volatile melt pool and keyhole. As a result, a temperature gradient was considered as a secondary effect and ommited in the 3D studies.

In summary, the 2D FEA models have provided valuable insight into the experimental results. Namely, ultrasound scattering was shown to scatter from the melt pool and keyhole tip and the effects of the liquid layer of the keyhole and temperature gradient in the solid. However, the 2D model does not fully capture the experimental setup, and care must be taken when directly comparing the two. For instance, the 2D model is simulating the cross section of an infinite, out-of-plane sample, which, in effect, make the keyhole an infinite crack. Additionally, the transmitter and receiver are aligned on the same plane, which is not representative of the experimental configuration and could lead to the received signal containing reflections from the sample surface. Therefore, to make a proper comparison to the experimental results and evaluate how ultrasound signals vary with the changing keyhole dimensions, a 3D model was used.

B. 3D model

For the 3D simulations, an $8 \times 6 \times 3$ mm geometry was selected with a structured mesh size of $8\,\mu$m as shown in Fig. 8. The keyhole was modeled with a width of $80\,\mu$m and depths ranging from 120 to $240\,\mu$m in $20\,\mu$m increments to simulate the various keyhole depths. As explained in Sec. II, the liquid layer surrounding the keyhole, as well as the temperature gradient in the solid, were both omitted in the 3D

model. The finite transducers used for excitation and reception were modeled to have a diameter of 2.5 mm. Appropriate delay laws were applied on the source nodes to focus the wave at the tip of a $180\,\mu$m keyhole. Similar to the experiments, the transmitter and receiver transducers are not on the same plane. An absorbing boundary of three wavelengths thickness was added along the surrounding surfaces normal to the x and y axes to minimise the internal boundary reflections. The FEA simulation was performed using Pogo, a graphics processing unit (GPU)-based finite-element solver, allowing up to 100 times the efficiency compared to central processing unit (CPU)-based solvers, enabling the simulation of large-scale models such as these.[31]

Generating shear waves travelling at a 45° angle from the excitation plane proved surprisingly tricky. One would expect that a straightforward usage of shear displacements coupled with the appropriate delay laws on the elements would suffice to accurately steer shear waves. However, in reality, this leads to poor beam forming primarily due to the directivity of the shear excitation source.[32] This is shown in Fig. 9 by using semi-infinite point source models and considering the resultant angular magnitudes of the shear waves excited from the appropriate point sources. With shear excitation, the angular range of the shear displacements is confined within ±50°, whereas longitudinal excitation allows the angular range of the shear displacements from approximately 30° to 40°. Therefore, 45° shear waves were generated and focused using appropriately time-delayed longitudinal excitation. Physically, this could be thought of as the oblique incident case at the solid–liquid interface beyond the first critical angle, where the pressure of the incident wave acts on the solid as normal, time-delayed forces
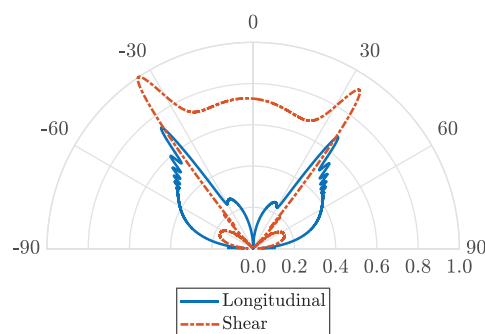

FIG. 9. (Color online) The shear wave directivity generated using the longitudinal and shear point excitation sources.

2416 J. Acoust. Soc. Am. **150** (4), October 2021
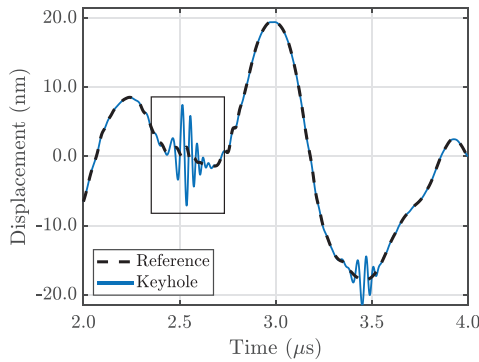
Gillespie *et al.*

FIG. 10. (Color online) The PC time-domain signals for the reference (without keyhole) and keyhole response. With the presence of the keyhole, the scattering signals are observed at 2.5 μs.

and results in refracted shear waves in the desired direction. It should be noted that in Fig. 9, the shear wave amplitude fluctuations generated using longitudinal excitation from 30° to 50° are mainly due to the presence of head waves, which cannot easily be isolated.[32] It should be noted that the directivity plots are slightly asymmetrical in amplitude as the excitation node in the model is located slightly off-center.

The raw time-domain signals for the PC configuration with and without the keyhole are shown in Fig. 10. The reference signal containing no keyhole can be seen to have large fluctuations. These fluctuations are due to modeling constraints whereby the finite source generates the surface waves, which propagate directly to the receiver. The scattering from the keyhole is found by subtracting the reference signal from the keyhole signal.

Using baseline subtraction, the scattered signals for both the PC and PE configurations can be calculated as shown in Fig. 11. In both configurations, an initial low amplitude response can be observed around 2.30–2.45 μs, followed by a high amplitude scattered signal. Similar to the TOFD, initial scattered signals are generated from the keyhole tip because the propagation length between the transducers and the tip is the shortest, resulting in a shorter TOF. In that regard, the high amplitude signals that occur later can likely be attributed to the cross-sectional area of the keyhole.

It is observed that the TOF of the low amplitude scattering from the tip decreases linearly with an increase in the keyhole depth while the amplitude remains constant. This reaffirms that the initial response from the tip behaves like a diffracted signal and can be used to provide information regarding the keyhole depth. For the range of keyhole depths considered, the low amplitude scattering has a linear change in the TOF of -0.5179 ns/μm. Furthermore, an analytical calculation was performed by dividing the propagation length with the shear wave velocity used. The analytical calculation predicts a theoretical change in the TOF of -0.4541 ns/μm, which is comparable to the finite-element results. However, whereas the low amplitude signals showed excellent correlation to the keyhole depth, such a signal (that changes in the TOF but not in the amplitude) was not observed in the experimental results. As a result, the high amplitude signals occurring after $t \approx 2.45$ μs were considered instead. A region of interest (ROI) was selected at $t \approx 2.5$ μs for both the PC and PE configurations as shown in Fig. 11. Further comparisons between the ROI of the finite-element and that of the experimental results will be made in Sec. IV.

In summary, both of the 2D and 3D FEA models were developed to answer several open questions from the experimental model. The 2D models were able to probe the effect of temperature and a liquid layer, namely, both can cause a decrease in the scattering amplitude and some phase shift in the signal depending on the configuration of the transducer. The 3D models were further able to highlight the effect that the keyhole depth has on both the TOF and amplitude.

IV. DISCUSSION AND CONCLUSION

The FEA results shown in Sec. III highlight the importance of the TOF and amplitude when considering the depth of the keyhole. Although the low amplitude signals were shown to be sensitive to the depth of the keyhole, such signals were not observed in the experimental results. This is likely a result of the high noise threshold that exists in the experiments, masking the low amplitude scattered signals. Moreover, the melt pools measured in the experiments are more complex and dynamic than the FEA models used, and the separation of the tip and the notch scattering may not be as well defined as that in the FEA models. Therefore, the high amplitude region at $t \approx 2.5$ μs was considered. A ROI in the FEA was selected based on similar criteria that was
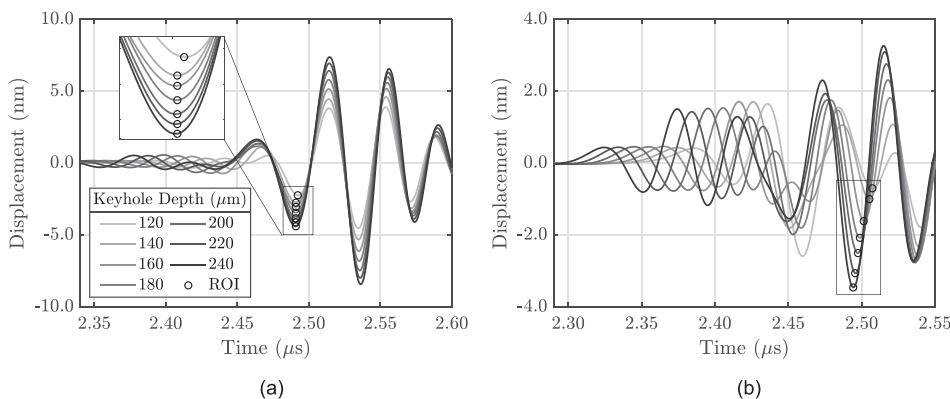

(a)

(b)

FIG. 11. The scattered signals from the keyhole with depths varying from 120 to 240 μm using the (a) PC and (b) PE configurations. The low amplitude signals prior to $t \approx 2.45$ μs are likely scattered from the tip of the keyhole, whereas later higher amplitude scattering is likely scattered from the cross-sectional area of the keyhole. The higher amplitude signals similar to those detected in the experimental measurements are highlighted in the region of interest (ROI).

J. Acoust. Soc. Am. **150** (4), October 2021

Gillespie *et al.*   2417

used in the experiments. As mentioned previously, the signal amplitude increases with the keyhole depth and is likely to be attributed to the cross-sectional area of the keyhole. The large signal after the initial peak is a result of scattering from the cross section of the keyhole that extends toward the surface of the sample. Because of a larger surface area than the tip, it scatters more energy and also arrives at a later time.

Whereas the experimental melt pool attained depths up to 400 μm, the digitizer was limited to a threshold of ± 1.2 V to increase the vertical resolution. During these greater depths, the amplitude of the ultrasonic scattering surpassed this threshold and the amplitudes were clipped. Consequently, only a melt pool and keyhole depth of 100–240 μm were considered in both the experimental and finite-element results, respectively, as no signal clipping occurred. Note, for the following analysis, the depths of the melt pool in the experiments and the keyhole in the finite-element simulations are treated as equivalent. The melt pool depths considered in the experiments correspond to the moment the keyhole initiates as seen in Fig. 3. At these depths, the amplitude of the ultrasonic scattering was below the digitizer threshold and, as a result, can be directly compared with the FEA results. Both the TOF and amplitude of the high amplitude scattering in the experiments and FEA are shown in Figs. 12(a) and 12(b), respectively.

Similar to the TOF, the relative amplitude shows a linear behavior with respect to the melt pool and keyhole depth. These results corroborate with previous work[21] that observed a linear change in the amplitude from ultrasonic scattering from the melt pool. Furthermore, the current results show this relationship is valid not only for melt pools but also during the keyhole initiation. For larger depths, the amplitude of the ultrasound was above the digitizer threshold and, therefore, not able to be analysed. Future work will need to address these shortcomings to consider the amplitude change during keyholing.

The experimental and FEA amplitudes exhibit a linear behavior for each configuration that is similar but not identical to the other. These results are not surprising between the two configurations as the PC and PE result in different portions of the scattered response being captured. However, it is interesting that the experimental configuration does not exhibit a similar behavior to that of the FEA. These differences can, again, likely be attributed to the temperature distribution and liquid layer present in the experimental configuration but not in the FEA. For the 2D simulations in Sec. III A, it was shown that both a temperature gradient and a liquid layer effectively dampen the ultrasonic wave and result in a lower scattering amplitude. This behavior is observed in Fig. 12(b), where the experimental change in amplitude is less than that of the FEA.

On the other had, the TOFs of the experiments show a linear relationship to the melt pool depth for both the PC and PE configurations, and the finite-element PC configuration does not show any relationship to the keyhole depth in the ROI considered. This could be due to the different keyhole shape used in the FEA as compared to the experimental melt pool shape. Nonetheless, the PE shows a linear relationship to the keyhole depth. On a whole, the experimental configuration experiences a greater change in the TOF as the simulation. These results make sense as the temperature gradient neglected in the finite element would slow the wave speed in the experiments and result in a greater TOF. Furthermore, because the experiments exhibit a linear response, it suggests that the temperature distribution in the heat-affected region has reached a steady-state relatively rapidly. These results are promising for future work to be able to determine a temperature correction factor to obtain quantitative melt pool measurements from the TOF.

It should be noted that whereas only the 100–240 μm region is considered in the current section, the linear TOF behavior extends to greater melt pool depths in the experimental configuration while the laser is active. Interestingly, after the laser turns off, a second linear TOF response was observed during cooling. This change in behavior is likely the result of the melt pool affecting the microstucture along with the porosity and hot cracking observed in the X-ray images.
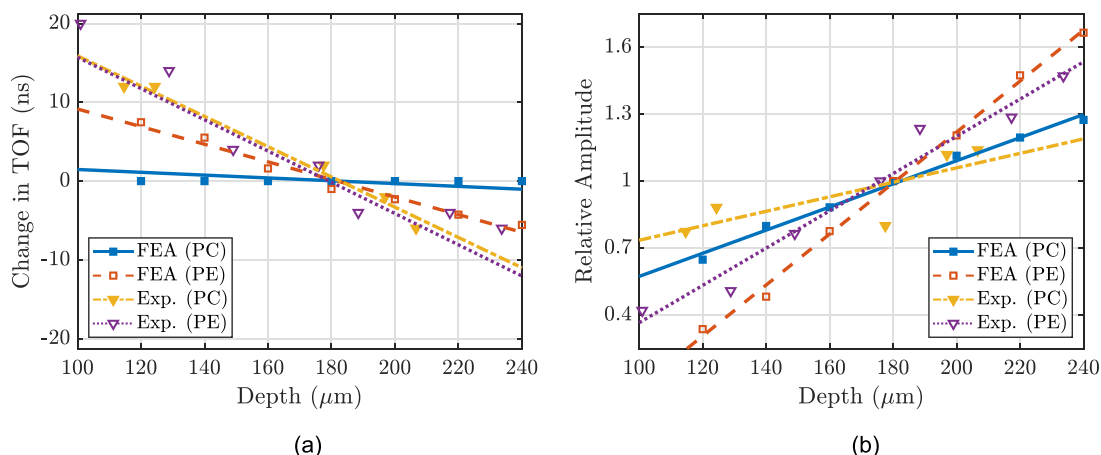
FIG. 12. (Color online) A (a) change in the TOF and (b) relative change in the amplitude with respect to the 180 μm depth. The FEA data correspond to the ROI in Fig. 11.

In conclusion, high-speed X-ray imaging was combined with immersion ultrasound to take synchronized measurements of laser-generated melt pools. The TOF of the scattering from the melt pool was shown to be highly sensitive to the depth of the melt pool. Furthermore, the 2D and 3D finite-element models were used to better interpret the scattering from the melt pool. The 2D simulations were able to study the effect that a temperature gradient and a liquid layer have on the scattering from the melt pool. Namely, both can cause a decrease in the amplitude and phase shift in the scattered signal. The 3D simulations were able to more accurately model the experimental simulations for a range of keyhole depths. These simulations indicate that early low amplitude scattering exists and is closely related to the scattering from the tip of the melt pools. Specifically, high amplitude scattering is thought to be related to the cross-sectional area of the keyhole. Due to the noise threshold in the experimental configuration, only the high amplitude regions were considered for both the experimental simulation and FEA. In this region, the change in the TOF and relative change in amplitude were shown to have a linear response to the depth of the melt pool and keyhole. Interestingly the high amplitude TOF in the FEA PC configuration did not appear to be significantly affected by the depth of the keyhole. It is currently unknown what is causing these differences. The FEA PE configuration did, however, show a similar response to that of the experimental configuration, abeit at a smaller change in the TOF. The larger change in the TOF in the experimental configuration is thought to caused by the temperature distribution in the heat-affected region slowing the wave velocity. Similarly, the difference between the relative change in amplitude between the experimental and finite-element models is thought to be due to the temperature distribution or liquid layer decreasing the scattering amplitude as seen in the 2D simulations.

The current work has provided promising results for the use of an ultrasound to characterize melt pools; however, several open questions remain for the experimental measurements as well as for the FEA simulations. First, the effects of a temperature gradient, although shown to affect the TOF, must be calculated to quantifiably measure the depths of the melt pool from the ultrasound measurements. Second, the difference in the response between the PC and PE configurations is still not entirely understood. A simultaneous measurement of the PC and PE for a single melt pool experiment may aid in this distinction as the melt pool behavior can be drastically different between experiments. It is noted that the low single-crystal anisotropy of aluminum[33] results in Al6061 being a weakly attenuating material relative to the other AM alloys such as the inconels and steels. In these other materials, a significant scattering of the ultrasound from the microscale grain boundaries will occur. The grain boundary scattering will compete with the scattered response from the melt pool, causing a reduction of the signal to noise.[34] However, the grain boundary scattering could be beneficial as it can possibly be used to characterize

the local microstructure that forms during the solidification.[35,36] Future configurations will take these materials into account by adjusting the ultrasonic frequency and offset distances. Future work involving additional experiments and more advanced FEA models can potentially address the open questions as well as help the method further evolve into a practical technology.

[1]T. DebRoy, H. L. Wei, J. S. Zuback, T. Mukherjee, J. W. Elmer, J. O. Milewski, A. M. Beese, A. Wilson-Heid, A. De, and W. Zhang, "Additive manufacturing of metallic components—Process, structure and properties," Prog. Mater. Sci. **92**, 112–224 (2018).

[2]M.-S. Pham, B. Dovgyy, P. A. Hooper, C. M. Gourlay, and A. Piglione, "The role of side-branching in microstructure development in laser powder-bed fusion," Nat. Commun. **11**, 749 (2020).

[3]B. P. Eftink, D. A. Vega, D. J. Sprouster, Y. S. J. Yoo, T. E. Steckley, E. Aydogan, M. Al-Sheikhly, T. J. Lienert, and S. A. Maloy, "Tensile properties and microstructure of additively manufactured grade 91 steel for nuclear applications," J. Nucl. Mater. **544**, 152723 (2021).

[4]W. E. King, H. D. Barth, V. M. Castillo, G. F. Gallegos, J. W. Gibbs, D. E. Hahn, C. Kamath, and A. M. Rubenchik, "Observation of keyhole-mode laser melting in laser powder-bed fusion additive manufacturing," J. Mater. Process. Technol. **214**(12), 2915–2925 (2014).

[5]C. Zhao, K. Fezzaa, R. W. Cunningham, H. Wen, F. De Carlo, L. Chen, A. D. Rollett, and T. Sun, "Real-time monitoring of laser powder bed fusion process using high-speed X-ray imaging and diffraction," Sci. Rep. **7**(1), 1–11 (2017).

[6]Z. Sun, X. Tan, C. Wang, M. Descoins, D. Mangelinck, S. B. Tor, E. A. Jägle, S. Zaefferer, and D. Raabe, "Reducing hot tearing by grain boundary segregation engineering in additive manufacturing: Example of an AlxCoCrFeNi high-entropy alloy," Acta Mater. **204**, 116505 (2021).

[7]N. Kouraytem, P.-J. Chiang, R. Jiang, C. Kantzos, J. Pauza, R. Cunningham, Z. Wu, G. Tang, N. Parab, C. Zhao, K. Fezzaa, T. Sun, and A. D. Rollett, "Solidification crack propagation and morphology dependence on processing parameters in AA6061 from ultra-high-speed x-ray visualization," Addit. Manuf. **42**, 101959 (2021).

[8]N. Tepylo, X. Huang, and P. C. Patnaik, "Laser-based additive manufacturing technologies for aerospace applications," Adv. Eng. Mater. **21**(11), 1900617–1900652 (2019).

[9]R. Cunningham, C. Zhao, N. Parab, C. Kantzos, J. Pauza, K. Fezzaa, T. Sun, and A. D. Rollett, "Keyhole threshold and morphology in laser melting revealed by ultrahigh-speed x-ray imaging," Science **363**(6429), 849–852 (2019).

[10]D. R. Clymer, J. Cagan, and J. Beuth, "Power-velocity process design charts for powder bed additive manufacturing," J. Mech. Des. Trans. ASME **139**(10), 100907 (2017).

[11]P. S. Cook and A. B. Murphy, "Simulation of melt pool behaviour during additive manufacturing: Underlying physics and progress," Addit. Manuf. **31**, 100909 (2020).

J. Acoust. Soc. Am. **150** (4), October 2021

Gillespie *et al.*   2419

26 November 2023 17:29:54

[12]S. K. Everton, M. Hirsch, P. I. Stavroulakis, R. K. Leach, and A. T. Clare, "Review of *in-situ* process monitoring and *in-situ* metrology for metal additive manufacturing," Mater. Des. **95**, 431–445 (2016).

[13]D.-H. Han, E. B. Flynn, C. R. Farrar, and L.-H. Kang, "A study on the *in-situ* melt pool size estimation method for directed-energy additive manufacturing based on modal parameters," 3D Pint Addit. Manuf. **6**, 99–112 (2019).

[14]N. D. Parab, C. Zhao, R. Cunningham, L. I. Escano, K. Fezzaa, W. Everhart, A. D. Rollett, L. Chen, and T. Sun, "Ultrafast X-ray imaging of laser–metal additive manufacturing processes," J. Synchrotron Radiat. **25**(5), 1467–1477 (2018).

[15]C. L. A. Leung, S. Marussi, R. C. Atwood, M. Towrie, P. J. Withers, and P. D. Lee, "*In situ* X-ray imaging of defect and molten pool dynamics in laser additive manufacturing," Nat. Commun. **9**(1), 1355 (2018).

[16]A. M. Kiss, A. Y. Fong, N. P. Calta, V. Thampy, A. A. Martin, P. J. Depond, J. Wang, M. J. Matthews, R. T. Ott, C. J. Tassone, K. H. Stone, M. J. Kramer, A. van Buuren, M. F. Toney, and J. Nelson Weker, "Laser-induced keyhole defect dynamics during metal additive manufacturing," Adv. Eng. Mater. **21**(10), 19004557 (2019).

[17]A. A. Martin, N. P. Calta, S. A. Khairallah, J. Wang, P. J. Depond, A. Y. Fong, V. Thampy, G. M. Guss, A. M. Kiss, K. H. Stone, C. J. Tassone, J. Nelson Weker, M. F. Toney, T. van Buuren, and M. J. Matthews, "Dynamics of pore formation during laser powder bed fusion additive manufacturing," Nat. Commun. **10**(1), 1987 (2019).

[18]C. Zhao, Q. Guo, X. Li, N. Parab, K. Fezzaa, W. Tan, L. Chen, and T. Sun, "Bulk-explosion-induced metal spattering during laser processing," Phys. Rev. X **9**(2), 021052 (2019).

[19]C. Zhao, N. D. Parab, X. Li, K. Fezzaa, W. Tan, A. D. Rollett, and T. Sun, "Critical instability at moving keyhole tip generates porosity in laser melting," Science **370**(6520), 1080–1086 (2020).

[20]J. J. Blecher, C. M. Galbraith, C. Van Vlack, T. A. Palmer, J. M. Fraser, P. J. Webster, and T. Debroy, "Real time monitoring of laser beam welding keyhole depth by laser interferometry," Sci. Technol. Weld. Join. **19**(7), 560–564 (2014).

[21]C. M. Kube, Y. Shu, A. J. Lew, and D. Galles, "Real-time characterization of laser-generated melt pools using ultrasound," Mater. Eval. **76**(4), 525–534 (2018).

[22]L. Schmerr, *Fundamentals of Ultrasonic Nondestructive Evaluation: A Modeling Approach* (Springer, Berlin, 2016).

[23]M. Matthews, J. Trapp, G. Guss, and A. Rubenchik, "Direct measurements of laser absorptivity during metal melt pool formation associated with powder bed fusion additive manufacturing processes," J. Laser Appl. **30**(3), 032302 (2018).

[24]P.-j. Chiang, R. Jiang, R. Cunningham, N. Parab, C. Zhao, K. Fezzaa, T. Sun, and A. D. Rollett, "*In situ* characterization of hot cracking using dynamic x-ray radiography," in *Advanced Real Time Imaging II* (2019), pp. 77–85.

[25]N. T. Aboulkhair, M. Simonelli, L. Parry, I. Ashcroft, C. Tuck, and R. Hague, "3D printing of aluminium alloys: Additive manufacturing of aluminium alloys using selective laser melting," Prog. Mater. Sci. **106**, 100578 (2019).

[26]C. T. Rueden, J. Schindelin, M. C. Hiner, B. E. DeZonia, A. E. Walter, E. T. Arena, and K. W. Eliceiri, "ImageJ2: ImageJ for the next generation of scientific image data," BMC Bioinf. **18**(1), 1–26 (2017).

[27]See supplementary material at https://www.scitation.org/doi/suppl/10.1121/10.0006386 for the video result showing simultaneous X-ray imaging and ultrasound in the pitch-catch mode as well as the video result showing simultaneous X-ray imaging and ultrasound in the pulse-echo mode.

[28]M. Smith, *ABAQUS/Standard User's Manual*, *Version 6.9* (Dassault Systèmes Simulia Corp., Providence, RI, 2009).

[29]J. A. Ogilvy and J. A. Temple, "Diffraction of elastic waves by cracks: Application to time-of-flight inspection," Ultrasonics **21**, 259–269 (1983).

[30]N. Saunders, X. Li, A. P. Miodownik, and J. Schille, "An integrated approach to the calculation of materials properties for ti-alloys," (2003), available at https://www.sentesoftware.co.uk/site-media/ti-jmatpro (Last viewed July 30, 2021).

[31]P. Huthwaite, "Accelerated finite element elastodynamic simulations using the GPU," J. Comput. Phys. **257**, 687–707 (2014).

[32]K. F. Graff, *Waves in Semi-Infinite Media* (Dover, New York, 1975), pp. 311–393, see https://books.google.com/books/about/Wave_Motion_in_Elastic_Solids.html?id=5cZFRwLuhdQC&source=kp_book_description.

[33]C. M. Kube, "Elastic anisotropy of crystals," AIP Adv. **6**, 095209 (2016).

[34]Y. Song, C. M. Kube, J. A. Turner, and X. Li, "Statistics associated with the scattering of ultrasound from microstructure," Ultrasonics **80**, 58–61 (2017).

[35]A. Wydra, A. M. Chertov, R. G. Maev, C. M. Kube, H. Du, and J. A. Turner, "Grain size measurement of copper spot welding caps via ultrasonic attenuation and scattering experiments," Res. Nondestruct. Eval. **26**, 225–243 (2015).

[36]A. P. Arguelles, C. M. Kube, P. Hu, and J. A. Turner, "Mode-converted ultrasonic scattering in polycrystals with elongated grains," J. Acoust. Soc. Am. **140**, 1570–1580 (2016).